Journal of
Composites Science

MDPI

Article

Polyamide Electrospun Nanofibers Functionalized with Silica and Titanium Dioxide Nanoparticles for Efficient Dye Removal

Safaa Saleh [1], Ahmed Salama [2], Ola M. Awad [1], Roberto De Santis [3], Vincenzo Guarino [3,*] and Emad Tolba [4]

[1] Department of Physics, Faculty of Science, Al-Azhar University (Girls Branch), Cairo P.O. Box 11884, Egypt
[2] Cellulose and Paper Department, National Research Centre, 33 El-Bohouth St., Dokki, Giza P.O. Box 12622, Egypt
[3] Institute of Polymers, Composites and Biomaterials, National Research Council of Italy, Mostra d'Oltremare, Pad.20, V.le J.F. Kennedy 54, 80125 Naples, Italy; rosantis@unina.it
[4] Polymers and Pigments Department, National Research Centre, 33 El-Bohouth St., Dokki, Giza P.O. Box 12622, Egypt; emad_nrc@yahoo.com
* Correspondence: vincenzo.guarino@cnr.it

Abstract: In this work, novel multifunctional electrospun nanofibrous membranes made of polyamide (PA6) and loaded with silica (SiO_2) and/or titanium dioxide (TiO_2) nanoparticles were fabricated. SiO_2 NPs were first prepared and then characterized by TEM, FE-SEM, and FTIR, and by using XRD techniques, confirming the formation of cristobalite tetragonal crystals with high purity. Different nanofibrous mats, loaded with SiO_2 NPs, TiO_2 NPs, or both SiO_2 and TiO_2 NPs, were investigated. Morphological studies indicated that SiO_2 and TiO_2 nanoparticles tend to be arranged along the fiber surface, also promoting the formation of anatase nanorods when they are mixed into the nanofibers. In this last scenario, mechanical tests have demonstrated that the presence of SiO_2 contributed to balancing the mechanical response of fibers that are negatively affected by the presence of TiO_2 NPs—as confirmed by tensile tests. More interestingly, the presence of SiO_2 did not negatively affect the antibacterial response against different bacteria populations (i.e., *Escherichia coli*, *Klebsiella pneumonia*, *Staphylococcus aureus*, *Bacillus subtilis*, and *Candida albicans*), which is mainly ascribable to the presence of TiO_2 particles. Accordingly, the TiO_2- and TiO_2/SiO_2-loaded fibers showed higher methylene blue (MB) absorption values—i.e., 26 mg/g and 27 mg/g—respectively, compared to the SiO_2-loaded fibers (23 mg/g), with kinetics in good agreement with the second-order kinetic model. The obtained findings pave the way for the formation of novel antibacterial membranes with a promising use in water purification.

Keywords: nanofibers; electrospinning; polyamide; titanium nanoparticles; dye removal

Citation: Saleh, S.; Salama, A.; Awad, O.M.; De Santis, R.; Guarino, V.; Tolba, E. Polyamide Electrospun Nanofibers Functionalized with Silica and Titanium Dioxide Nanoparticles for Efficient Dye Removal. *J. Compos. Sci.* **2024**, *8*, 59. https://doi.org/10.3390/jcs8020059

Academic Editors: Ahmed Koubaa, Mohamed Ragoubi and Frédéric Becquart

Received: 8 January 2024
Revised: 18 January 2024
Accepted: 29 January 2024
Published: 4 February 2024

1. Introduction

The purification of highly polluted colored wastewater is now considered one of the major concerns to environmental health. One of the most serious worldwide problems that threatens human health is water contamination [1,2]. Daily, water resources including oceans, rivers, lakes, and groundwater are being contaminated by various toxic pollutants [3]. These pollutants may include inorganic and organic materials, nanoparticles, microbes, pathogens, oil, dyes, heavy metals, and different heavy pollutants [4–6]. As a result, millions of people die annually from diseases related to unsafe water. Therefore, there is an urgent need for the application of low-cost water purification methods to ensure pure drinking water. Photocatalysis technology using semiconductors has attracted widespread scientific attention as a promising approach for solving this problem, as the photoactive species can decompose a variety of organic pollutants that are present in water [7–11]. Various approaches have been planned for organic dye elimination, including biodegradation, coagulation, and adsorption, with different benefits and drawbacks [11]. Due to its convenient operation and reduced environmental impacts, adsorption has been considered an effective and economical technique. Various adsorbents, including zeolite [12],

carbon [13], polymers [14], and composites, have been demonstrated to be useful for dye removal. Among them, organic/inorganic composites outperform other materials due to their high surface area, high thermal stability, and easy modification [15,16]. Recently, one of the most high-performance adsorbents that can avoid most of the problems related to traditional adsorbents has been identified as nanofibrous polymers. Due to the high surface area and 3D structure, nanofibrous adsorbents exhibit higher activity and a decreased time of transfer of the reactants from the material bulk into active sites. In this context, electrospinning is one of the most important processing methods for the fabrication of composite ultrafine fibers, with average diameters ranging from a few to hundreds of nanometers [17]. In this technique, a special polymeric solution is injected into a nozzle under the effect of a strong electrostatic field [18]. When applying the electrostatic field, the charges formed on the surface of the droplet by surface tension will induce the formation of a jet that will be stretched, forming ultrafine fibers. These formed nanofibrous mats have a large surface area and a porous structure [19,20]. Different natural and synthetic polymers have been applied for the formation of electrospun fibers; one of these polymers is polyamide (PA6). Polyamide is a synthetic biocompatible and biodegradable polymer with good mechanical properties [21]. Polyamide can be dissolved in a formic or formic/acetic solution and is resistant to water and humidity. Therefore, recent research has addressed the use of polyamide for use in the filtration process [22,23].

In addition to the special features offered by electrospun nanofibers for application in water purification, it is important to improve their filtration performance by surface functionalization [24]. This can be achieved by introducing nanoparticles, such as ZnO and TiO_2, or by the co-introduction of nanoparticles that further improve the adsorption ability. These nanoparticles exhibit good physiochemical properties and a high surface area [25]. They play an important role in the dissociation of heavy pollutants present in water, due to the presence of functional groups that are considered good adsorbents of heavy metals and organic pollutants [24,26].

This work aims to introduce titanium oxide and silica nanoparticles into electrospun nanofibers. Titanium oxide (TiO_2) or titania has become increasingly important in recent years since the observation of its role in the photo-assisted electrochemical splitting of water in 1972 [10,27]. TiO_2 has attracted much attention as it can improve the hydrophilicity of nanofibers, accelerate the interactions between water and membranes, and even has the capability to inhibit certain bacteria [28]. In nature, titania is known to have three different polymorphs, namely, rutile, anatase, and brookite [29]. Anatase is most widely used in photocatalysis, due to the negative potential of its conduction band, which enables this phase to be efficient in redox reactions [30]. SiO_2 is an amorphous material with a large surface area, high thermal stability, non-toxicity, and stable chemical properties; hence, it can be employed as an excellent carrier material [31]. Silica nanoparticles can be used in different applications, such as filtration, biosensors, energy saving, and drug delivery. Also, the presence of SiO_2 inside nanofibers can enhance their wettability and their tensile strength [31].

However, for most applications of nanofibers loaded with SiO_2, most of the silica nanoparticles are coated with the polymer layer, which limits the functions of these loaded nanoparticles. As a result, a novel method is needed to solve this problem.

Several studies have been conducted on the functionalization of membranes by different methods to improve their efficiency in water purification. Jinyuan Zhu et al. [32] triggered a photocatalyst process starting from activated carbon loaded with fluorine and silica-doped TiO_2. In this process, TiO_2 is present on the surface and shows a significant absorption activity toward methylene blue (MB) dye. Recently, Akmal Zulfi et al. [33] prepared electrospun membranes, based on polyvinyl chloride loaded with in situ silver and TiO_2 nanoparticles. In this case, the photocatalytic effect was related to degradation under visible light and was coupled with a reduction in fiber diameter. In this regard, Firas J. Kadhim et al. [34] recently proposed using a reactive magnetron sputtering technique to

produce photocatalysts from TiO_2/SiO_2, with the results exhibiting higher dye absorption efficiency compared to TiO_2 alone.

The present work aims to prepare novel electrospun fibers loaded with SiO_2 and TiO_2 for water purification. In this study, SiO_2 nanoparticles will be synthesized via the sol-gel method. A novel method is optimized to functionalize electrospun nanofibers by loading SiO_2 and TiO_2 nanoparticles. The membranes will be characterized using different techniques, and their use will be validated in terms of their performance against different microbes and the adsorption of MB dye.

2. Materials and Methods

2.1. Materials

Sodium silicate, polyethylene oxide (PEO, MW 600 kDa), titanium isopropoxide, and polyamide (PA6) were all purchased from Sigma–Aldrich (Milan, Italy). Distilled water, formic acid, and absolute ethanol ($\geq$99.5%) were also utilized in this work. All chemicals were of analytical grade and were used as received, without further purification.

2.2. Synthesis of SiO_2 Nanoparticles

The SiO_2 nanoparticles were synthesized using the sol-gel method. Typically, 4.73 g of sodium silicate was dissolved by stirring in 60 mL of distilled water. Then, 0.1 g of PEO was dissolved in 15 mL of ethanol. After that, the PEO solution was titrated into the SiO_2 solution. The mixed solution was stirred for about 1 h. The pH of the solution was adjusted at two different values to examine the influence of the pH on the morphology of the nanoparticles; these values are 1 and 7. This mixed solution was aged for about 1 week, then washed and centrifuged at about 5000 rpm. Finally, it was calcined at about 700 °C for about 1 h.

2.3. Preparation of PA Electrospun Solution

Nanofibrous mats were prepared using a custom-made electrospinning device. Herein, 25% w/v of PA6 was prepared in a formic acid solution. Then, the electrospinning process was conducted, involving the application of 20 kV at a 1 mL/h flow rate, with 12 cm of distance between the tip of the needle and the collector, for a 5 h collection time and using a needle gauge of 19. The rotating drum was used as the collector. This sample was named P.

2.4. Preparation of Nanofibrous Mats Loaded with Silica (SiO_2) NPs

PA6 solution (25%) was prepared in the formic acid, then 2% of the previously prepared powder containing SiO_2 nanoparticles was added. The mixture was then stirred for 2 h and sonicated for 20 min to ensure good dispersion of the nanoparticles. This solution was electrospun under the same conditions as discussed above. This sample was named PS.

2.5. Preparation of Nanofibrous Mats Loaded with Titanium Dioxide (TiO_2) NPs

For the introduction of TiO_2 into the nanofibrous mat, the PA6 nanofibrous mat (P sample) was soaked in a solution containing the titanium isopropoxide precursor and ethanol (1:9 v/v). The soaked mats were left for 1 day, then dipped out from the solution, cleaned several times with distilled water, and dried for further application. The code for this sample was PT.

2.6. Preparation of Nanofibrous Mats Loaded with Both SiO_2 and TiO_2 Nanoparticles

The previously prepared PA6 fibrous mats loaded with SiO_2 nanoparticles (PS sample) were soaked in a solution containing the titanium isopropoxide precursor and ethanol (1:9 v/v). The mats were soaked for 1 day, then dipped out from the solution, cleaned several times with distilled water, and dried for further application. The code of this sample was PST.

2.7. Characterization

The morphology of the SiO_2 nanoparticles and prepared nanofibrous mats was examined by FE-SEM (JSM 6360LV, JEOL, Tokyo, Japan). The elemental composition analysis of the nanofibrous mats was performed by EDX, coupled with SEM. Also, the morphology of the SiO_2 NPs was examined by TEM (JeolJem-1230, JEOL, Tokyo, Japan). Fourier transform infrared spectroscopy (FTIR) analysis of all the samples (nanoparticles and nanofibers) was performed by Jasco, FTIR—6100 type A (Lisses, France). The FTIR spectra were obtained in the region of 4000–400 cm^{-1} for all samples. Phase analysis of the prepared samples (nanoparticles and nanofibers) was applied using an X-ray diffractometer Bruker D8 advance CuK target, with a secondary monochromator at 40 kV and 40 mA.

2.8. Mechanical Testing

Mechanical properties were measured through tensile tests. Specimens were cut using the Ceast cutting machine, equipped with an ASTM D1708 cutting die. Each specimen's thickness was measured through a non-contact laser sensor (Micro-Epsilon optoNCDT 1420-10, MICRO-EPSILON UK & Ireland Ltd., Ortenburg, Germany). Tensile tests were performed using the Bose Electroforce Test Bench System, equipped with a 25 N cell load. The elongation speed was set at 1 mm/min. Stress and strain were obtained by dividing the load and the elongation by the specimen's cross-section area and the initial length, respectively. The elastic modulus was determined through the stress vs. strain diagrams by measuring the curve's steepness in the linear region. An analysis of variance, followed by Tukey's test at a significant level of 0.05, was carried out to assess statistical differences among the samples.

2.9. Antimicrobial Activity

2.9.1. Microorganism and Growth Conditions

Five selected pathogens were utilized for investigating the antimicrobial activity of the different nanofibrous samples (P, PT, and PST). These pathogens included Gram-negative bacteria (*Escherichia coli* ATCC 8739 and *Klebsiella pneumonia* ATCC13883), Gram-positive bacteria (*Staphylococcus aureus* ATCC 6538 and *Bacillus subtilis* ATCC 6633), and fungi (*Candida albicans* ATCC 10221). The microbial strains were cultivated in test tubes containing 5 mL of Mueller–Hinton broth composed of (%): 0.2 beef extract, 1.75 acid hydrolysate of casein, and 0.15 starch, under starting cultivation (200 rpm) for one day at 37 °C. The antimicrobial performance of different samples was assessed using a disk diffusion approach.

2.9.2. Disk Diffusion Technique

The disk diffusion approach was used to assess the antimicrobial activity of the prepared samples [35]. In brief, 100 µL of serially diluted pathogens was separately distributed on Petri dishes containing Mueller–Hinton agar medium, along with disks (8 mm in diameter) from the nanofibrous mat. To complete the diffusion of the tested samples as well as to inhibit the model microbes, all the plates were left at 4 °C for 120 min and were subsequently incubated for 1 day at 37 °C. Then, after the incubation period, the inhibition-zone diameter was estimated to evaluate the antibacterial activity. The electrospun mats were sterilized for 30 min under UV before application. All experiments were performed in triplicate and the resulting means were represented.

2.10. Adsorption Studies

The prepared PS, PT, and PST nanofibrous mats were examined for use as adsorbents for organic dye removal from wastewater. The adsorption experiments were carried out at 25 °C, using the depletion method. The suspension, containing 50 mg of PS, PT, and PST mats, was soaked in 50 mL MB solution. The kinetics were evaluated, with 60 mg/L as the initial dye concentration and at a pH fixed at 7. Experiments were carried out after 24 h to determine the complete adsorption isotherm. Different concentration solutions of

MB (10–100 ppm) were prepared. According to the following equation, the amount of MB adsorbed in the solution, q_e (mg/g), was determined after adsorption:

$$q_e = ((C_o - C_e)V)/m \quad (1)$$

Here, the initial and equilibrium concentrations of the dye (measured in mg/L) are denoted by C_o and C_e, respectively. During the adsorption experiment, V represents the volume of MB (measured in L) and m represents the mass of the nanofibers.

3. Results and Discussion

3.1. Characterization of Silica-Nanoparticles

The effect of pH value on the morphology of the formed SiO_2 NPs before and after calcination is illustrated in Figure 1. The nanoparticles prepared at pH 7 (Figure 1b,d) showed a well-defined spherical shape compared to the nanoparticles prepared at pH 1 (Figure 1a,c). Therefore, this value of pH was selected for the preparation of SiO_2 NPs and applied in further work. It is also noted that calcination aids in the improvement of the shape, crystallinity, and photocatalytic effect of the nanoparticles, which can also be enhanced by calcination as it reduces recombination between the holes and negative electrons [32].

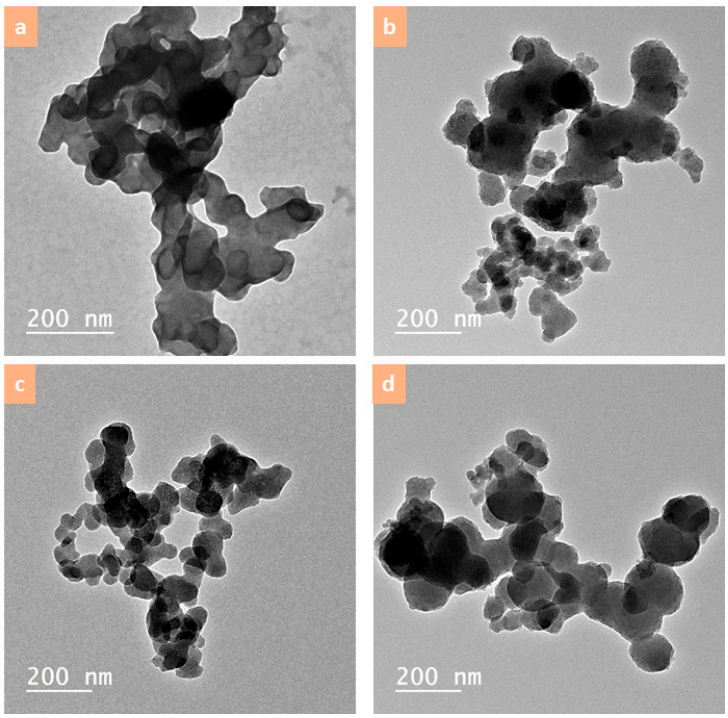

Figure 1. TEM images of SiO_2 NPs prepared at pH 1—before (**a**) and after (**c**) calcination—and at pH 7 before (**b**) and after (**d**) calcination.

The FE-SEM images of the calcined SiO_2 NPs prepared at pH 7 are shown at two different magnifications in Figure 2a,b. The image at high magnification shows the formation of interconnected rough spheres, with several internal gaps. The structure and purity of the formed SiO_2 NPs are shown in Figure 2c, which illustrates the FTIR spectrum of the prepared SiO_2 NPs. The band at about 1083 cm^{-1} corresponds to the asymmetric stretching vibration of the Si-O-Si (siloxane) bond [33–36]. The band at about 800 cm^{-1} refers to the presence of the vibrational mode of the Si-OH (silanol) bond [37–39]. At about 450 cm^{-1}, the band may be attributed to the asymmetric rocking vibration produced by the Si-O-Si bond [36,40]. The absence of any other peaks emphasizes the purity of the formed Si NPs. The phase analysis of the formed SiO_2 NPs was examined using XRD (Figure 1d). The diffraction lines were compared with the standards and were found to match the cristobalite

tetragonal phase (SiO_2), according to the card number (ICDD No. 01-082-0512). Diffraction peaks were noted at 2θ 21.76°, 31.62°, 35.9°, 45.33°, 56.36°, and 66.17°.

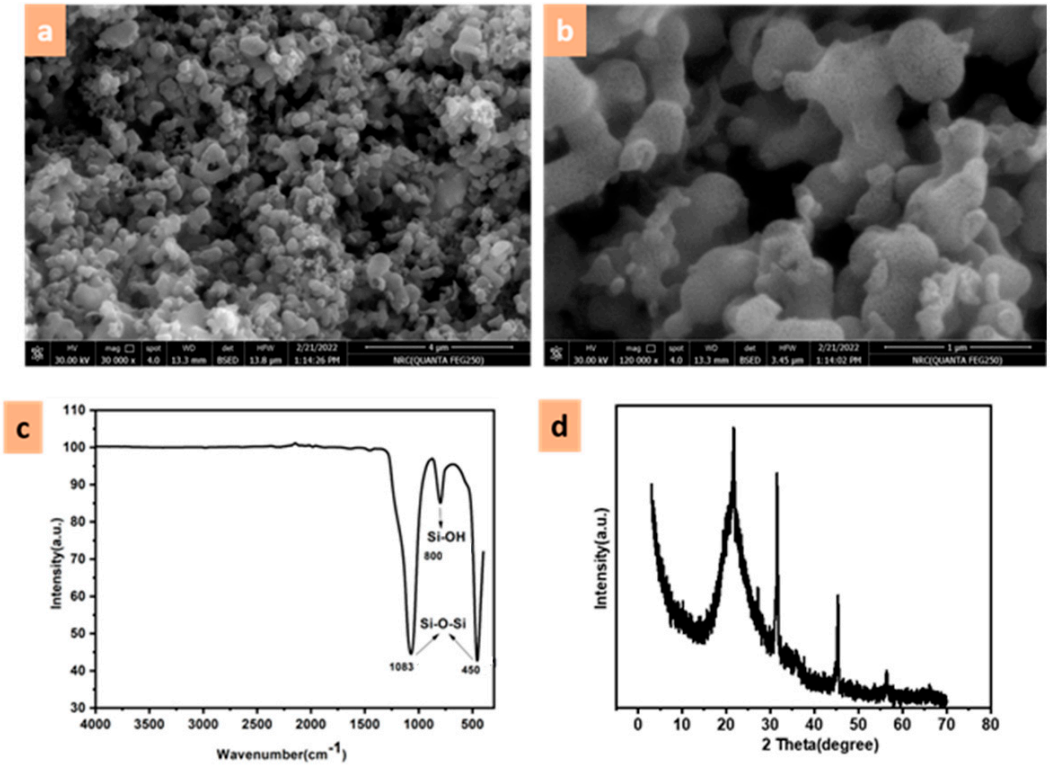

Figure 2. Calcinated SiO_2 NP characterization: (**a**,**b**) FE-SEM images of the calcined samples at pH 7, with the (**c**) FTIR image and (**d**) XRD spectra.

3.2. Characterization of Electrospun Nanofibers Loaded with Nanoparticles

Figure 3 illustrates the FE-SEM images of neat PA6 nanofibers (A,B), fibers loaded with silica nanoparticles (D,E), fibers loaded with TiO_2 nanoparticles (G,H), and those loaded with SiO_2 and TiO_2 nanoparticles (J,K).

All the images confirm the presence of heterogeneous beadless fibers with an average fiber diameter of nearly 200 ± 25 nm for neat nanofibers, 100 ± 73 nm for nanofibers loaded with SiO_2, and 150 ± 30 nm for those loaded with TiO_2, while the mean diameter for nanofibers loaded with both SiO_2 and TiO_2 was about 135 ± 44 nm. The absence of beads improved the quality of the nanofibrous mats as the surface area of the sheet was improved and was then ready to receive any incorporated materials. Fibers loaded with SiO_2 showed the existence of SiO_2 NPs as grain-like structures agglomerated on the surface of the nanofibers. Figure 3G,H shows the FE-SEM of nanofibers loaded with TiO_2 NPs and emphasizes the good distribution of TiO_2 nanoparticles, which cover all the surfaces of the fibers. Compared to fibers loaded with SiO_2 nanoparticles, the fibers loaded with TiO_2 nanoparticles possessed a high ratio of loading of the TiO_2 nanoparticles on the surface of the nanofibers; this may be due to good adhesion between the nanofibers and TiO_2 nanoparticles. For fibers loaded with both SiO_2 and TiO_2 nanoparticles, Figure 3J,K shows that the surface of the nanofibers was completely covered by Ti nanorods with interconnected pores. This may be due to the presence of SiO_2 NPs on the fibers, playing a role in converting loaded Ti from nanoparticles to nanorods.

Figure 3C,F,I,L show the EDX elemental analysis for the different samples. Figure 3C confirms the purity of the neat polyamide electrospun nanofibers, which exhibited the C, N, and O elements related to PA6. Figure 3F underlines the presence of Si NPs on the surface of the nanofibers, while Figure 3I illustrates the existence of Ti NPs on the surface of the nanofibers. Figure 3L confirms the high ratio of the Ti element deposited on the surface

of the nanofibers. These results reflect the role of SiO_2 NPs in the high deposition of Ti nanorods on the surface of the nanofibers.

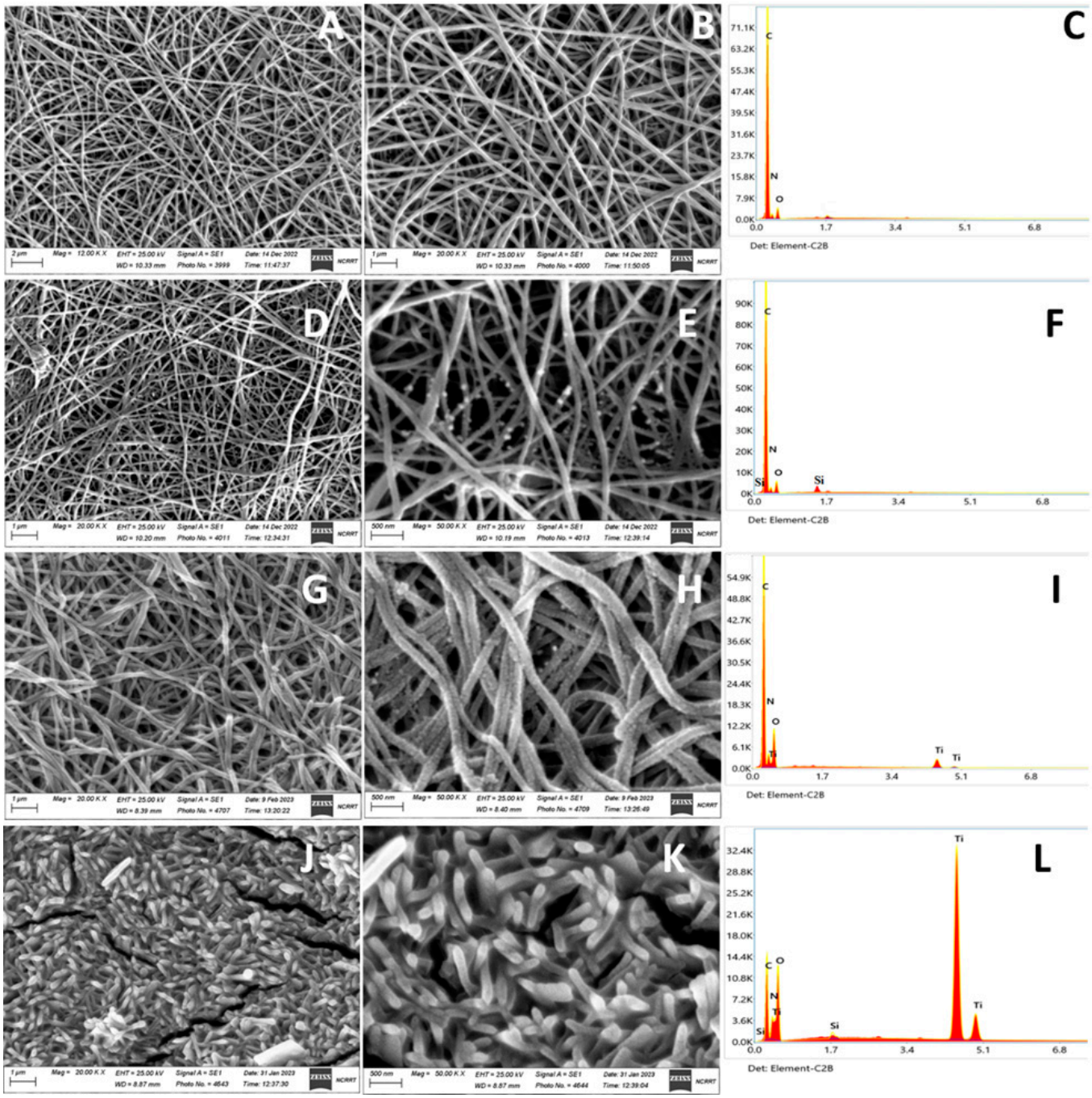

Figure 3. Morphological investigation of the fibrous membranes via FE-SEM: (**A**,**B**) P sample, (**D**,**E**) PS sample, (**G**,**H**) PT sample, and (**J**,**K**) PST sample and EDX spectra respectively (**C**,**F**,**I**,**L**).

The structural features of the electrospun PA6 nanofibrous mats were confirmed via FT-IR analyses (Figure 4).

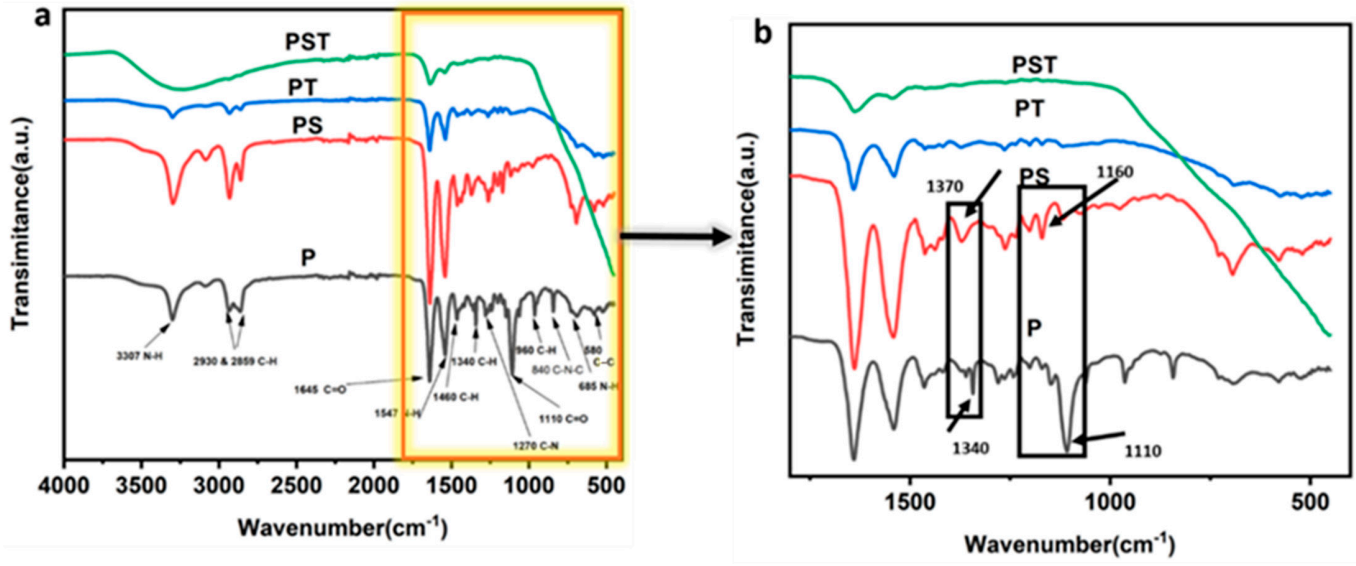

Figure 4. (**a**) FTIR spectra of the P, PS, PT, and PST samples, (**b**) magnification of the spectrum between 1800 and 1400 cm^{-1}.

The spectra show a band at about 3307 cm^{-1}, which can be assigned to the stretching vibration of N-H, while the peaks that appeared at 2930 and at 2859 are related to the asymmetric vibration of the C-H group [41,42]. At 1645 cm^{-1}, the band is related to the C=O stretching vibration of the amide bond, and at 1547 cm^{-1}, the band is crossed to the N-H absorption peak of the amide group [43]. At 1460 cm^{-1}, the band represents the CH_2 bending vibration, while at 1340 cm^{-1}, the band is related to the CH_2 deformation vibration [44,45]. The band occurring at 1260 cm^{-1} is assigned to the C-N elongation band and the band at 1110 cm^{-1} represents the C=O stretching vibration. The weak bands at 960 and 840 cm^{-1} are due to the C-H vibration and C-N-C scissor vibration, respectively, while at 685 cm^{-1}, the band can be attributed to the N-H out-of-plane bending vibration. The weak band at about 580 cm^{-1} can be attributed to C-C elongation [46].

Figure 4b shows a magnification of the spectrum between 1800 and 400 cm^{-1} to focus on the details in this region. As illustrated, the spectrum of the PS sample (nanofibers loaded with SiO_2 NPs) exhibited most of the major peaks of PA6. However, there are some variations due to the introduction of SiO_2 NPs into the nanofibers. The peaks at 3307, 2930, 2859, 1645, 1547, and 685 cm^{-1} increased in intensity, while the peaks at 960 and 840 cm^{-1} diminished to a significant extent with the introduction of SiO_2 NPs. The peak at 1340 shifted to 1370 cm^{-1} and the peak at 1110 cm^{-1} also decreased in intensity and shifted to 1160 cm^{-1}. All these variations reflect the interaction between the SiO_2 NPs and PA6.

The spectrum of the PT sample—i.e., the sample loaded with TiO_2 NPs—indicates that the presence of TiO_2 NPs caused a higher decrease in intensity of peaks at 3307, 2930, 2859, and 1645 cm^{-1} and the absence of most of the peaks between 1480 and 800 cm^{-1}. These changes were due to the presence of TiO_2 NPs with a high ratio on the polymer surface, influencing all the peaks related to PA6.

The introduction of both SiO_2 and TiO_2 NPs—see the PST spectrum—caused the presence of a broad band centered at 3248 cm^{-1} and a significant decrease in intensity of the peaks at 1645 and at 1547 cm^{-1}, with the absence of all other peaks related to polyamide. These may be due to overlapping between the peaks related to PA6 and TiO_2. The differences between the spectra of the PT and PST samples may reflect variations in the morphology of TiO_2 nanoparticles.

Crystalline phases in the fibers were also characterized using XRD. Figure 5a shows two main different diffraction peaks at 2θ 13.7° and 16.5°, which are associated with the γ phase (pseudo-hexagonal) form of PA6, while the α phase form (monoclinic) can be observed at 2θ 21.22°, representing the mesomorphic β form of PA6 [47]. The characteristic

peaks of PA6 can also be recognized in all the diffractograms of the PA6 composite fibers loaded with NPs. Figure 5b relates to the spectrum of the PS sample and indicates the presence of a diffraction peak at 23.4° that belongs to amorphous SiO_2 NPs [48]. The spectrum of the PT sample (Figure 5c) emphasizes the presence of the anatase phase, which is confirmed by the presence of a peak at 37.77° (101 plane), while the spectrum of the PST sample illustrates the presence of a peak at 23.4° that shows the presence of SiO_2 and also a peak at 25.1° (004 plane) related to anatase [49,50]. The results of the XRD analysis confirm the successful loading of NPs into the nanofibrous mats; the phase of TiO_2 is anatase, which is important in applications for water purification due to its photocatalytic effect [30]. Also, the presence of SiO_2 NPs in the fibers changed the plane of growth of the TiO_2 NPs from the 101 plane to the 004 plane; this may illustrate the change in the shape of the TiO_2 NPs from nanoparticles (PT sample) to nanorods (PST sample) [11].

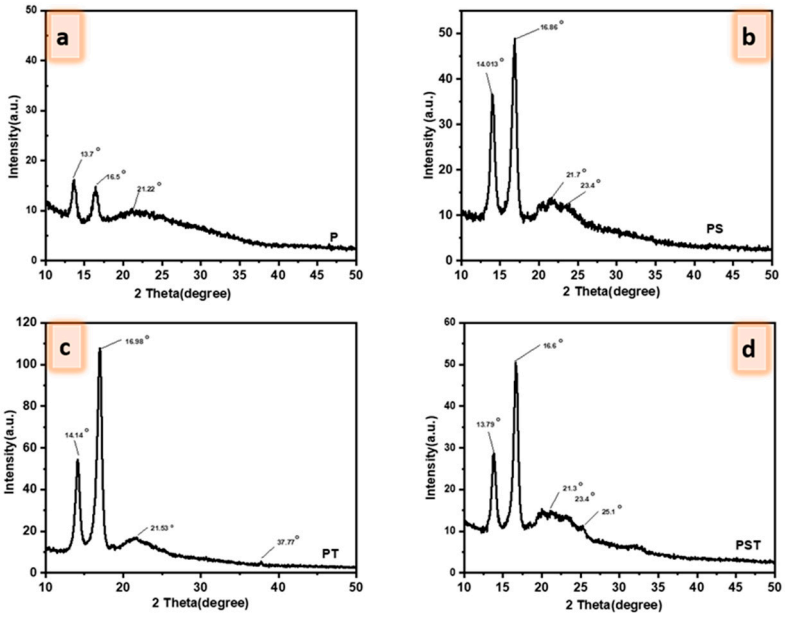

Figure 5. XRD analysis: spectra of the (**a**) P, (**b**) PS, (**c**) PT, and (**d**) PST samples. The peaks at 23.4° and 37.77° are related to the amorphous SiO_2 and TiO_2 phases. An additive peak at 25.1° (anatase) is also apparent in the case of PST.

3.3. Mechanical Properties

Figure 6 shows the tensile behavior and mechanical properties of the investigated samples. All samples displayed an almost linear behavior (Figure 6a). The behavior of the pristine PA6 sample is almost consistent with previous widely documented uniaxial tensile tests [51–56]; any differences mainly depend on the electrospinning process parameters, porosity, and elongation speed. Very little is known about the stress vs. strain curves of PA6 electrospun nanofibers loaded with TiO_2, SiO_2, and TiO_2/SiO_2 NPs. However, a significant reduction in the steepness (i.e., the stiffness) of the linear region and a significant decrease in the breaking point (i.e., the strength) has been observed for PA6/TiO_2 [55].

The elastic modulus of electrospun nanofibers is a mechanical property of paramount importance as it determines the geometrical stability of polymer-based membranes for water purification [16] and the softness of COVID-19 masks [55]. Moreover, in the case of tissue engineering, the membrane's stiffness plays an important role in the activation of cellular mechano-transduction pathways [57]. The stiffness (i.e., the elastic modulus reported in Figure 6b) of the PA6 sample (51.4 ± 4.8 MPa) was significantly higher ($p < 0.05$) than that of PA6/TiO_2 (39.3 ± 2.9 MPa). Therefore, the incorporation of TiO_2 NPs reduced the stiffness of PA6 by 23%. The stiffness values reported for PA6 and PA6/TiO_2 are consistent with those deduced from the stress vs. strain curves reported by Deyab et al. [55]. Conversely, the stiffness of PA6/SiO_2 (59.9 ± 4.7 MPa) was significantly higher

than that of PA6 ($p < 0.05$). Therefore, the incorporation of SiO_2 NPs increased the stiffness of PA6 by about 17%. Interestingly, for the PA6/TiO_2/SiO_2 sample, the silica NPs balanced out the stiffness reduction due to TiO_2 NPs.

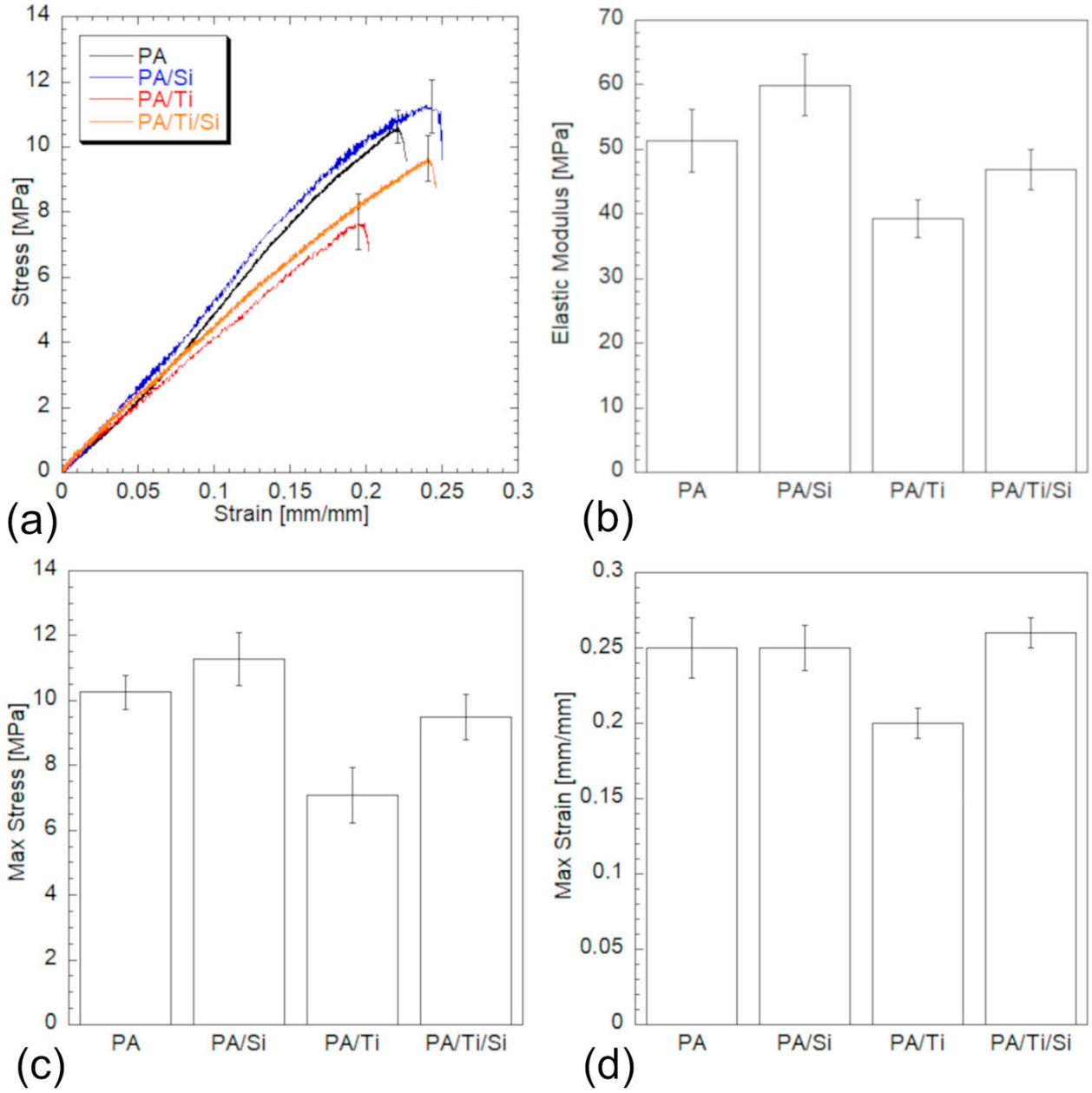

Figure 6. Mechanical properties of the P, PS, PT, and PST samples. (**a**) The stress vs. strain curves, (**b**) elastic modulus, (**c**) maximum stress, and (**d**) maximum strain.

A similar effect of the NP-loaded PA6 nanofibers can be observed regarding the maximum stress (Figure 6c). Of course, the maximum stress (i.e., the strength) is also a mechanical property of paramount importance, as it represents the maximum load that an electrospun membrane can withstand. A strength increase of 11% was recorded once the SiO_2 NPs were embedded into the PA6 fibers. However, this increase is not statistically significant. Higher strength values were measured by Islam et al. for both PA6 and Pa6/SiO_2 electrospun membranes [58]. This inconsistency may be due to the adopted elongation speed and the higher amount of silica NPs ($20\%_{w/w}$). The maximum stress of the PA6/TiO_2 sample (7.1 ± 0.8 MPa) is significantly lower ($p < 0.05$) than those of all the other investigated samples. In particular, TiO_2 NPs reduce the strength of the PA6 membrane by 31%.

A higher strength reduction (of about 50%) was observed by Islam et al. [58]. Again, for the PA6/TiO_2/SiO_2 sample, silica NPs allow the balancing of the strength reduction due to TiO_2 NPs.

The maximum strain (i.e., the compliance) of the investigated electrospun membranes is depicted in Figure 6d. The effect of SiO_2 NPs on the compliance of PA6-based membranes was negligible. Instead, a significant compliance reduction ($p < 0.05$) of 20% was observed because the TiO_2 NPs were used alone.

3.4. Antibacterial Effect

Nanofibrous mats (P, PT, andPTS) were tested for antimicrobial activity. Table 1 and Figure 7 show the inhibition zone diameter (mm) of the samples against different tested microorganisms. This test was performed against Gram-positive bacteria (*Bacillus subtilis* and *Staphylococcus aureus*) and Gram-negative bacteria (*Escherichia coli* and *Klebsiella pneumonia*), as well as antifungal activity (*Candida albicans*).

The pure PA6 nanofibrous mat (P sample) did not exhibit any effects against all tested microbes except for *Candida albicans*. For all other samples (PT and PST), an inhibition zone was noted against all tested microorganisms. For *Bacillus subtilis*, higher microbial activity was noted for PT than for PTS. For *Staphylococcus aureus* and *Escherichia coli*, a greater influence was recorded for the PST sample, followed by the PT sample. For *Klebsiella pneumonia*, the most pronounced influence was noticed for PST, then for PT. For *Candida albicans*, the higher microbial influence was recorded for PT, followed by PST, and the lowest effect was noticed for the P sample. For all samples, a higher microbial effect was noted for Gram-positive bacteria than for Gram-negative bacteria, and finally for *Candida albicans*.

From these results, it is clear that the presence of TiO_2 inside the nanofibers induced their antibacterial behavior. This may be due to TiO_2 nanoparticles being able to promote the inactivation of microorganisms due to their strong oxidizing power, by generating free radicals such as anionic hydroxyl and superoxide radicals [59].

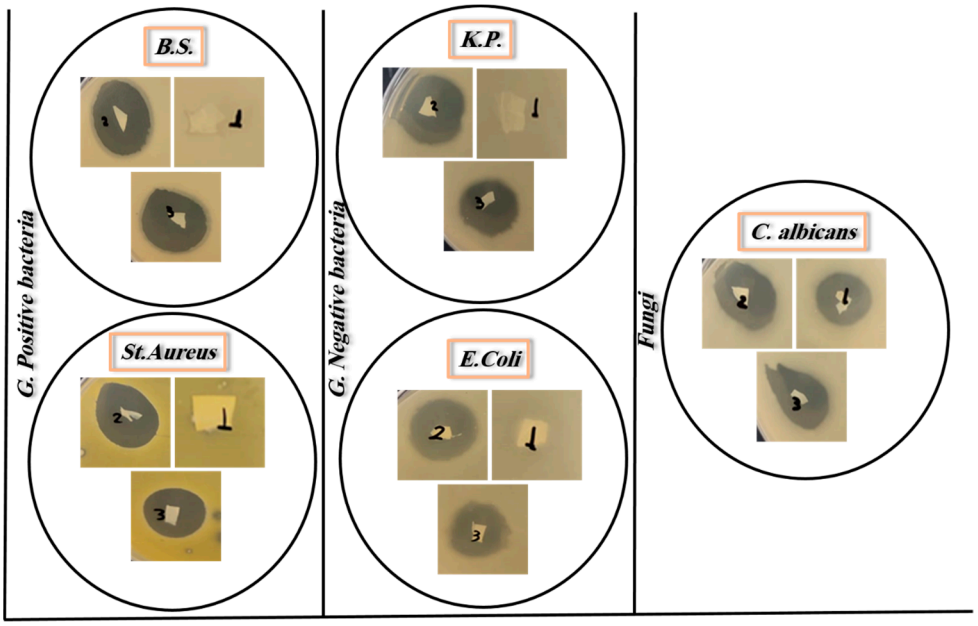

Figure 7. Antimicrobial effect against Bacillus subtilis, *Staphylococcus aureus, Escherichia coli, Klebsiella pneumonia,* and *Candida albicans* of the P (1), PST (2), and PT (3) samples.

Table 1. Inhibition zone diameter (mm) of the samples. NA: no effect was recorded.

		Sample		
		Diameter of Inhibition Zone (mm)		
Pathologic Microorganisms		CTR	PST	PT
Gram-positive	*Bacillus subtilis*	NA	25 ± 0.125	26 ± 0.155
	Staphylococcus aureus	NA	23 ± 0.279	20 ± 0.425
Gram-negative	*Escherichia coli*	NA	22 ± 0.371	20 ± 0.526
	Klebsiella pneumonia	NA	25 ± 0.293	22 ± 0.783
Fungi	*Candida albicans*	17 ± 0.24	19 ± 0.529	23 ± 0.631

3.5. Methylene Blue (MB) Adsorption

Many industrial dyes are toxic, mutagenic, and even carcinogenic. Today, a new material is needed for wastewater dye removal applications. The purpose of this study was to examine the removal of MB from water by nanofibrous mats synthesized from PS, PT, and PST. Adsorbents can be used to remove dye from aqueous solutions, but this depends on several factors, including pH and equilibrium time.

3.5.1. Effect of Contact Time and Adsorption Kinetics

This experiment was conducted to examine the effect of contact time on the adsorption performance of PS, PT, and PST nanofibrous mats. Over a specified period of contact time, these materials were evaluated for their MB dye adsorption capacity. The results revealed that the dye adsorption rate for PS, PT, and PST samples was rapid within the first 80 min of contact time, as presented in Figure 8. There may have been free active sites on the surface of the materials that promoted rapid adsorption. Furthermore, equilibrium was reached after approximately 120 min. These results demonstrate that the adsorption capacity of PT and PST was higher than that of PS. As a result, the experiment focused on the impact of contact time and the composition of the nanofibers on their properties and their potential applications in a variety of fields, such as wastewater treatment and environmental remediation.

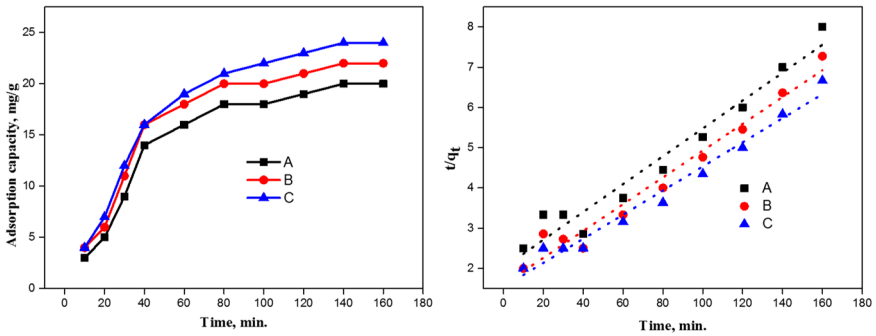

Figure 8. Effect of time on the adsorption capacity of MB (**Left**) and pseudo-second-order kinetic model linear fitting (**Right**) for PS (A), PT (B), and PST (C).

The kinetic results of MB adsorption onto the PS, PT, and PST samples were examined by two kinetic models, i.e., the pseudo-first-order and pseudo-second-order models (Equations (2) and (3)).

$$\log\ (q_e - q_t) = \log(q_e) - \frac{K_1}{2.303} t \quad (2)$$

$$t/q_t = t/q_e + 1/K_2 q_e^2 \quad (3)$$

Here, q_t (mg/g) represents the amount of adsorption over time, while q_e (mg/g) refers to the amount of adsorption at equilibrium. The rate constants of the pseudo-first-order and pseudo-second-order models are denoted as K_1 (min^{-1}) and K_2 (g mg^{-1} min^{-1}), respectively.

Table 2 shows the factors of the kinetic models for the three prepared composite fibers. Based on the pseudo-second-order models, the calculated q_e values for the PS, PT, and PST samples are 28.6, 30, and 33.5 mg/g, respectively. These values are close to the experimental q_e computations (20, 22, and 24 mg/g), and the correlation coefficients (R2) are approximately 0.95, 0.97, and 0.97, for the PS, PT, and PST samples, respectively. Therefore, a good fit of the kinetic data with the pseudo-second-order model is demonstrated. These findings suggest that chemical bonds between the MB and the fibers control adsorption.

Table 2. Kinetic parameters for MB adsorption by the PS, PT, and PST samples.

	Pseudo-First-Order Parameters				Pseudo-Second-Order Parameters		
	$q_{e.exp}$ (mg/g)	$q_{e.cal}$ (mg/g)	K1 (min^{-1})	R2	q_e.cal (mg/g)	K_2 (g(mg min)$^{-1}$)	R^2
PS	20	89	1.2×10^{-3}	0.74	28.6	6.07×10^{-4}	0.95
PT	22	88	1.3×10^{-3}	0.73	30	6.96×10^{-4}	0.97
PST	24	87	1.4×10^{-3}	0.79	33.5	5.82×10^{-4}	0.97

3.5.2. Effect of MB Concentration and Adsorption Isotherms

Figure 9 displays the relationship between the initial MB concentration and the adsorption capacity of the PS, PT, and PST samples. By increasing the concentration of MB in the solution, the driving force for the transfer of MB from the aqueous to the solid phase is enhanced, improving the adsorption of MB onto nanofiber active sites. The removal of MB increased up to 20, 23, and 24 mg/g in the PS, PT, and PST samples, respectively, when the MB content was 100 ppm. At around 60 mg/g, the maximum adsorption showed a plateau due to the saturation of the active sites for the prepared fibers. To optimize the adsorption process, the behavior of dye molecules needs to be understood at the solid–liquid interface. In addition to providing information about adsorption capacities and equilibrium concentrations, adsorption isotherms also provide information about adsorbent and adsorbate interactions. In the current study, the adsorption isotherms of the PS, PT, and PST samples were evaluated to establish their potential use for adsorption. Besides providing information about homogeneous adsorption, the Langmuir isotherm also indicates that a monolayer has formed. The Freundlich isotherm describes heterogeneous and multilayer surface phenomena. Equations (4) and (5) correspond to the Langmuir and Freundlich isotherms, respectively.

$$\frac{C_e}{q_e} = \frac{K_s}{q_{\max}} + \frac{C_e}{q_{\max}} \tag{4}$$

$$\log q_e = \frac{1}{n} \log C_e + \log P \tag{5}$$

The amount of MB adsorbed by the hydrogel (in mg/g) is represented by q_e, while C_e refers to the equilibrium concentration of the dye (in mg/L). q_{max} (in mg/g) represents the highest amount of MB that can be adsorbed on the fibers, and K_s (in mg/L) represents the Langmuir constant. The capacity of adsorption (in mg/g) is represented by P, while n is a constant that describes the intensity of adsorption (dimensionless).

As shown in Table 3, the Langmuir isotherm reported a higher correlation coefficient for the adsorption of MB dye molecules onto the PS, PT, and PST samples, representing the formation of a monolayer of the dye that directly interacts with the surface of the fibers. According to the Langmuir isotherm, the adsorption efficiency of the PS, PT, and PST samples was recorded at 23, 26, and 27 mg/g, respectively. Accordingly, Table 4 compares the maximum adsorption efficiency of dyes by different adsorbents.

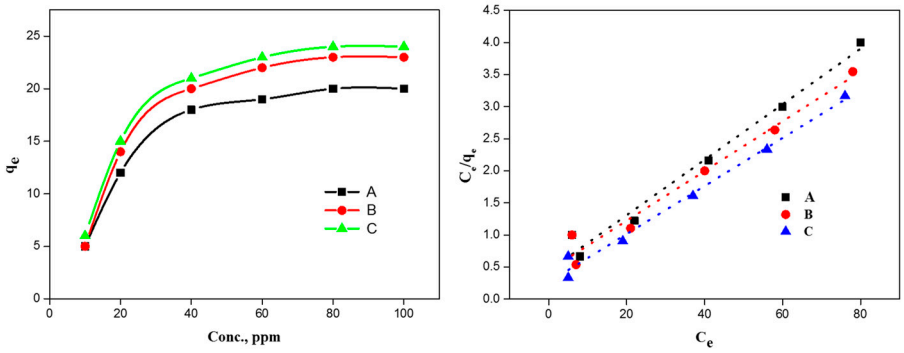

Figure 9. Effect of the concentration of MB on the adsorption (**Left**) and curves of the isothermal Langmuir model (linear fitting) (**Right**) for PS (A), PT (B), and PST (C).

Table 3. Different equilibrium models for the adsorption of MB on the PS, PT, and PST samples.

	Langmuir Isotherm Parameters			Freundlich Isotherm Parameters		
	K_s (mg/L)	q_m (mg/g)	R^2	P (mg/g)	n	R^2
PS	10.28	23	0.98	3.63	2.32	0.71
PT	11.6	26	0.97	3.71	2.28	0.68
PST	7.1	27	0.98	5.71	2.72	0.63

Table 4. Comparison of the performance of the different reported sorbents for dye removal.

Adsorbent	Adsorption Efficiency mg/g	References
Freshly prepared manganese dioxide	627.1	[60]
Natural lignocellulosic	244.6	[2]
Magnetic mesoporous silica	208.31	[15]
Raw and activated red mud	5.86	[61]
Wheat straw	131.123	[62]
Polydopamine-coated hydrogen titanate nanowires	586.7	[63]
Activated carbon derived from sucrose and melamine	454.57	[64]
Polyamide loaded with silica oxide and/or titanium dioxide	27	This study
Ficus palmata leaves	6.89	[65]

4. Conclusions

In the present study, a new type of antibacterial nanofibrous membrane was prepared by electrospinning. SEM observation showed a uniform fiber morphology with characteristic sizes in the sub-micrometric range, with an increase in average fiber diameters due to the presence of both NPs. The FTIR results also confirmed an interaction between loaded NPs and PA6 fibers. TiO_2 NPs significantly reduce the stiffness, strength, and compliance of PA6 nanofibers. Instead, SiO_2 NPs increase the stiffness and strength. In the case of loading PA6 nanofibers with both NPs, silica NPs allow the balancing of the stiffness, strength, and compliance reduction that is ascribed to TiO_2 NPs. Meanwhile, the combined presence of SiO_2 and TiO_2 improved the adsorption capacity of methylene blue onto the fiber surface, with the isothermal adsorption curves being fully consistent with the Langmuir model. The kinetic equation was consistent with the pseudo-second-order kinetic equation, demonstrating that the chemical adsorption is the rate control step. Lastly, a higher microbial effect was noticed in the presence of SiO_2 and TiO_2 for Gram-positive

and Gram-negative bacteria and *Candida albicans*. Unsurprisingly, this is ascribable to the recognized antibacterial response of TiO_2, against different bacteria populations, but this is not limited to/compromised by the presence of SiO_2. All the results suggest an interesting use for SiO_2- and TiO_2-loaded nanofibers as a functional antibacterial membrane for applications in water purification.

Author Contributions: E.T. and S.S. conceived the work. A.S., O.M.A., V.G. and R.D.S. performed the experiments and wrote the preparation section. V.G. supervised the work. All authors have read and agreed to the published version of the manuscript.

Funding: The National Research Council (CNR) of Italy and the Egyptian Academy of Scientific Research and Technology gave their financial support through the Joint Bilateral Agreement (Biennial Program 2022–2023).

Data Availability Statement: Data are contained within the article.

Conflicts of Interest: The authors declare no conflicts of interest.

References

1. Wu, X.Q.; Shao, Z.D.; Liu, Q.; Xie, Z.; Zhao, F.; Zheng, Y.M. Flexible and porous TiO_2/SiO_2/carbon composite electrospun nanofiber mat with enhanced interfacial charge separation for photocatalytic degradation of organic pollutants in water. *J. Colloid Interface Sci.* **2019**, *553*, 156–166. [CrossRef] [PubMed]
2. Mosoarca, G.; Popa, S.; Vancea, C.; Dan, M.; Boran, S. Removal of Methylene Blue from Aqueous Solutions Using a New Natural Lignocellulosic Adsorbent—Raspberry (*Rubus idaeus*) Leaves Powder. *Polymers* **2022**, *14*, 1966. [CrossRef] [PubMed]
3. Khulbe, K.C.; Matsuura, T. Art to use electrospun nanofibers/nanofiber based membrane in waste water treatment, chiral separation and desalination. *J. Membr. Sci. Res.* **2019**, *5*, 100–125. [CrossRef]
4. Adam, M.R.; Othman, M.H.D.; Kurniawan, T.A.; Puteh, M.H.; Ismail, A.F.; Khongnakorn, W.; Rahman, M.A.; Jaafar, J. Advances in adsorptive membrane technology for water treatment and resource recovery applications: A critical review. *J. Environ. Chem. Eng.* **2022**, *10*, 107633. [CrossRef]
5. Nayl, A.A.; Abd-Elhamid, A.I.; Awwad, N.S.; Abdelgawad, M.A.; Wu, J.; Mo, X.; Gomha, S.M.; Aly, A.A.; Bräse, S. Review of the Recent Advances in Electrospun Nanofibers Applications in Water Purification. *Polymers* **2022**, *14*, 1594. [CrossRef] [PubMed]
6. Jamil, T.; Munir, S.; Wali, Q.; Shah, G.J.; Khan, M.E.; Jose, R. Water Purification through a Novel Electrospun Carbon Nanofiber Membrane. *ACS Omega* **2021**, *6*, 34744–34751. [CrossRef] [PubMed]
7. Dong, S.; Feng, J.; Fan, M.; Pi, Y.; Hu, L.; Han, X.; Liu, M.; Sun, J.; Sun, J. Recent developments in heterogeneous photocatalytic water treatment using visible light-responsive photocatalysts: A review. *RSC Adv.* **2015**, *5*, 14610–14630. [CrossRef]
8. Göktaş, R.K.; MacLeod, M. Remoteness from sources of persistent organic pollutants in the multi-media global environment. *Environ. Pollut.* **2016**, *217*, 33–41. [CrossRef]
9. Song, Y.; Zhao, F.; Li, Z.; Cheng, Z.; Huang, H.; Yang, M. Electrospinning preparation and anti-infrared radiation performance of silica/titanium dioxide composite nanofiber membrane. *RSC Adv.* **2021**, *11*, 23901–23907. [CrossRef]
10. Gaidau, C.; Petica, A.; Ignat, M.; Popescu, L.M.; Piticescu, R.M.; Tudor, I.A.; Piticescu, R.R. Preparation of silica doped titania nanoparticles with thermal stability and photocatalytic properties and their application for leather surface functionalization. *Arab. J. Chem.* **2017**, *10*, 985–1000. [CrossRef]
11. Al-Hamoud, K.; Shaik, M.R.; Khan, M.; Alkhathlan, H.Z.; Adil, S.F.; Kuniyil, M.; Assal, M.E.; Al-Warthan, A.; Siddiqui, M.R.H.; Tahir, M.N.; et al. Pulicaria undulata extract-mediated eco-friendly preparation of TiO_2 nanoparticles for photocatalytic degradation of methylene blue and methyl Orange. *ACS Omega* **2022**, *7*, 4812–4820. [CrossRef]
12. Habiba, U.; Siddique, T.A.; Li Lee, J.J.; Joo, T.C.; Ang, B.C.; Afifi, A.M. Adsorption study of methyl orange by chitosan/polyvinyl alcohol/zeolite electrospun composite nanofibrous membrane. *Carbohydr. Polym.* **2018**, *191*, 79–85. [CrossRef] [PubMed]
13. He, X.; Male, K.B.; Nesterenko, P.N.; Brabazon, D.; Paull, B.; Luong, J.H.T. Adsorption and desorption of methylene blue on porous carbon monoliths and nanocrystalline cellulose. *ACS Appl. Mater. Interfaces* **2013**, *5*, 8796–8804. [CrossRef] [PubMed]
14. Salama, A. Preparation of CMC-g-P(SPMA) super adsorbent hydrogels: Exploring their capacity for MB removal from waste water. *Int. J. Biol. Macromol.* **2018**, *106*, 940–946. [CrossRef] [PubMed]
15. Nicola, R.; Muntean, S.-G.; Nistor, M.-A.; Putz, A.-M.; Almásy, L.; Săcărescu, L. Highly efficient and fast removal of colored pollutants from single and binary systems, using magnetic mesoporous silica. *Chemosphere* **2020**, *261*, 127737. [CrossRef] [PubMed]
16. Matos, J.; Ocares-Riquelme, J.; Poon, P.S.; Montaña, R.; Garcia, X.; Campos, K.; Hernández-Garrido, J.C.; Titirici, M.M. C-doped anatase TiO_2: Adsorption kinetics and photocatalytic degradation of methylene blue and phenol, and correlations with DFT estimations. *J. Colloid Interface Sci.* **2019**, *547*, 14–29. [CrossRef] [PubMed]
17. Guarino, V.; Cruz-Maya, I.; Altobelli, R.; Abdul Khodir, W.K.; Ambrosio, L.; Alvarez Pèrez, M.A.; Flores, A.A. Electrospun polycaprolactone nanofibres decorated by drug loaded chitosan nano-reservoirs for antibacterial treatments. *Nanotechnology* **2017**, *28*, 505103. [CrossRef]

18. Gohary, M.I.E.; Hady, B.M.A. El Saeed, A.A.A.; Tolba, E.; Rashedi, A.M.I.E.; Saleh, S. Electrospinning of doxorubicin loaded silica/poly(ϵ-caprolactone) hybrid fiber mats for sustained drug release. *Adv. Nat. Sci. Nanosci. Nanotechnol.* **2018**, *9*, 2. [CrossRef]
19. Vineis, C.; Cruz Maya, I.; Mowafi, S.; Varesano, A.; Sánchez Ramírez, D.O.; Abou Taleb, M.; Tonetti, C.; Guarino, V.; El-Sayed, H. Synergistic effect of sericin and keratin in gelatin based nanofibers for in vitro applications. *Int. J. Biol. Macromol.* **2021**, *190*, 375–381. [CrossRef]
20. Renkler, N.Z.; Cruz-Maya, I.; Bonadies, I.; Guarino, V. Electro Fluid Dynamics: A Route to Design Polymers and Composites for Biomedical and Bio-Sustainable Applications. *Polymers* **2022**, *14*, 4249. [CrossRef]
21. Matulevicius, J.; Kliucininkas, L.; Martuzevicius, D.; Krugly, E.; Tichonovas, M.; Baltrusaitis, J. Design and characterization of electrospun polyamide nanofiber media for air filtration applications. *J. Nanomater.* **2014**, *2014*, 859656. [CrossRef]
22. Aydin-Aytekin, D.; Gezmis-Yavuz, E.; Buyukada-Kesici, E.; Cansoy, C.E.; Alp, K.; Koseoglu-Imer, D.Y. Fabrication and characterization of multifunctional nanoclay and TiO_2 embedded polyamide electrospun nanofibers and their applications at indoor air filtration. *Mater. Sci. Eng. B* **2022**, *279*, 115675. [CrossRef]
23. Žagar, E.; Češarek, U.; Drinčić, A.; Sitar, S.; Shlyapnikov, I.M.; Pahovnik, D. Quantitative Determination of PA6 and/or PA66 Content in Polyamide-Containing Wastes. *ACS Sustain. Chem. Eng.* **2020**, *8*, 11818–11826. [CrossRef]
24. Gao, X.; Li, Z.K.; Xue, J.; Qian, Y.; Zhang, L.Z.; Caro, J.; Wang, H. Titanium carbide Ti_3C_2Tx (MXene) enhanced PAN nanofiber membrane for air purification. *J. Memb. Sci.* **2019**, *586*, 162–169. [CrossRef]
25. Wahid, F.; Zhao, X.-Q.; Cui, J.-X.; Wang, Y.-Y.; Wang, F.-P.; Jia, S.-R.; Zhong, C. Fabrication of bacterial cellulose with TiO_2-ZnO nanocomposites as a multifunctional membrane for water remediation. *J. Colloid Interface Sci.* **2022**, *620*, 1–13. [CrossRef] [PubMed]
26. Salama, A. Recent progress in preparation and applications of chitosan calcium phosphate composite materials. *Int. J. Biol. Macromol.* **2021**, *178*, 240–252. [CrossRef] [PubMed]
27. Albukhaty, S.; Al-Bayati, L.; Al-Karagoly, H.; Al-Musawi, S. Preparation and characterization of titanium dioxide nanoparticles and in vitro investigation of their cytotoxicity and antibacterial activity against Staphylococcus aureus and Escherichia coli. *Anim. Biotechnol.* **2022**, *33*, 864–870. [CrossRef]
28. Feng, X.; Zhang, S.; Wu, H.; Lou, X. A novel folic acid-conjugated TiO_2-SiO_2 photosensitizer for cancer targeting in photodynamic therapy. *Colloids Surf. B Biointerfaces* **2015**, *125*, 197–205. [CrossRef]
29. Tachikawa, T.; Fujitsuka, M.; Majima, T. Mechanistic insight into the TiO_2 photocatalytic reactions: Design of new photocatalysts. *J. Phys. Chem. C* **2007**, *111*, 5259–5275. [CrossRef]
30. Zhang, J.; Zhou, P.; Liu, J.; Yu, J. New understanding of the difference of photocatalytic activity among anatase, rutile and brookite TiO_2. *Phys. Chem. Chem. Phys.* **2014**, *16*, 20382–20386. [CrossRef]
31. Shahhosseininia, M.; Bazgir, S.; Joupari, M.D. Fabrication and investigation of silica nanofibers via electrospinning. *Mater. Sci. Eng. C* **2018**, *91*, 502–511. [CrossRef]
32. Gupta, K.; Singh, R.P.; Pandey, A.; Pandey, A. Photocatalytic antibacterial performance of TiO_2 and Ag-doped TiO_2 against S. Aureus. P. Aeruginosa and E. Coli. *Beilstein J. Nanotechnol.* **2013**, *4*, 345–351. [CrossRef]
33. Feifel, S.C.; Lisdat, F. Silica nanoparticles for the layer-by-layer assembly of fully electro-active cytochrome c multilayers. *J. Nanobiotechnol.* **2011**, *9*, 59. [CrossRef] [PubMed]
34. Zaharudin, N.S.; Mohamed Isa, E.D.; Ahmad, H.; Abdul Rahman, M.B.; Jumbri, K. Functionalized mesoporous silica nanoparticles templated by pyridinium ionic liquid for hydrophilic and hydrophobic drug release application. *J. Saudi Chem. Soc.* **2020**, *24*, 289–302. [CrossRef]
35. Saleh, S.; Salama, A.; Ali, A.M.; Saleh, A.K.; Elhady, B.A.; Tolba, E. Egyptian propolis extract for functionalization of cellulose nanofiber/poly (vinyl alcohol) porous hydrogel along with characterization and biological applications. *Sci. Rep.* **2023**, *13*, 7739. [CrossRef]
36. Saravanan, S.; Dubey, R.S. Synthesis of SiO_2 nanoparticles by sol-gel method and their optical and structural properties. *Rom. J. Inf. Sci. Technol.* **2020**, *23*, 105–112.
37. Mehmood, Y.; Khan, I.U.; Shahzad, Y.; Khalid, S.H.; Asghar, S.; Irfan, M.; Asif, M.; Khalid, I.; Yousaf, A.M.; Hussain, T. Facile synthesis of mesoporous silica nanoparticles using modified sol-gel method: Optimization and in vitro cytotoxicity studies. *Pak. J. Pharm. Sci.* **2019**, *32*, 1805–1812.
38. Darmakkolla, S.R.; Tran, H.; Gupta, A.; Rananavare, S.B. A method to derivatize surface silanol groups to Si-alkyl groups in carbon-doped silicon oxides. *RSC Adv.* **2016**, *6*, 93219–93230. [CrossRef]
39. Shawky, S.M.; Abo-AlHassan, A.A.; Lill, H.; Bald, D.; EL-Khamisy, S.F.; Ebeid, E.-Z.M. Efficient Loading and Encapsulation of Anti-Tuberculosis Drugs using Multifunctional Mesoporous Silicate Nanoparticles. *J. Nanosci. Curr. Res.* **2016**, *1*, 1–9. [CrossRef]
40. Gui-Long, X.; Changyun, D.; Yun, L.; Pi-hui, P.; Jian, H.; Zhuoru, Y. Preparation and characterization of raspberry-like SiO_2 particles by the sol-gel method. *Nanomater. Nanotechnol.* **2011**, *1*, 79–83. [CrossRef]
41. Bahrami, M.; Abenojar, J.; Martínez, M.A. Comparative characterization of hot-pressed polyamide 11 and 12: Mechanical, thermal and durability properties. *Polymers* **2021**, *13*, 3553. [CrossRef]
42. Kang, E.; Kim, M.; Oh, J.S.; Park, D.W.; Shim, S.E. Electrospun BMIMPF 6/Nylon 6,6 nanofiber chemiresistors as organic vapour sensors. *Macromol. Res.* **2012**, *20*, 372–378. [CrossRef]
43. Sridhara, P.K.; Masso, F.; Olsén, P.; Vilaseca, F. Strong polyamide-6 nanocomposites with cellulose nanofibers mediated by green solvent mixtures. *Nanomaterials* **2021**, *11*, 2127. [CrossRef]

44. Al-Deyab, S.S.; El-Newehy, M.H.; Nirmala, R.; Abdel-Megeed, A.; Kim, H.Y. Preparation of nylon-6/chitosan composites by nanospider technology and their use as candidate for antibacterial agents. *Korean J. Chem. Eng.* **2013**, *30*, 422–428. [CrossRef]
45. Ndesendo, V.M.K.; Choonara, Y.E.; Meyer, L.C.R.; Kumar, P.; Tomar, L.K.; Tyagi, C.; Du Toit, L.C.; Pillay, V. In vivo evaluation of a mucoadhesive polymeric caplet for intravaginal anti-HIV-1 delivery and development of a molecular mechanistic model for thermochemical characterization. *Drug Dev. Ind. Pharm.* **2015**, *41*, 1274–1287. [CrossRef]
46. Oulidi, O.; Nakkabi, A.; Elaraaj, I.; Fahim, M.; Moualij, N. El Incorporation of olive pomace as a natural filler in to the PA6 matrix: Effect on the structure and thermal properties of synthetic Polyamide 6. *Chem. Eng. J. Adv.* **2022**, *12*, 100399. [CrossRef]
47. Farias-Aguilar, J.C.; Ramírez-Moreno, M.J.; Téllez-Jurado, L.; Balmori-Ramírez, H. Low pressure and low temperature synthesis of polyamide-6 (PA6) using Na0 as catalyst. *Mater. Lett.* **2014**, *136*, 388–392. [CrossRef]
48. Sun, J.; Xu, Z.; Li, W.; Shen, X. Effect of Nano-SiO_2 on the Early Hydration of Alite-Sulphoaluminate Cement. *Nanomaterials* **2017**, *3*, 102. [CrossRef] [PubMed]
49. Wei, X.; Zhu, G.; Fang, J.; Chen, J. Synthesis, characterization, and photocatalysis of well-dispersible phase-pure anatase TiO_2 nanoparticles. *Int. J. Photoenergy* **2013**, *2013*, 726872. [CrossRef]
50. Jameel, Z.N.; Haider, A.J.; Taha, S.Y. Synthesis of TiO_2 Nan particles by Using Sol-Gel Method and its Applications as Antibacterial Agents. *Eng. Tech. J.* **2014**, *418*, 3–4. [CrossRef]
51. Bazbouz, M.B.; Stylios, G.K. The tensile properties of electrospun nylon 6 single nanofibers. *J. Polym. Sci. B Polym. Phys.* **2010**, *48*, 1719–1731. [CrossRef]
52. Mannarino, M.M.; Rutledge, G.C. Mechanical and tribological properties of electrospun PA 6 (3) T fiber mats. *Polymer* **2012**, *53*, 3017–3025. [CrossRef]
53. Wu, S.; Wang, B.; Zheng, G.; Liu, S.; Dai, K.; Liu, C.; Shen, C. Preparation and characterization of macroscopically electrospun polyamide 66 nanofiber bundles. *Mater. Lett.* **2014**, *12*, 77–80. [CrossRef]
54. Zhao, J.; Zhu, W.; Wang, X.; Liu, L.; Yu, J.; Ding, B. Fluorine-free waterborne coating for environmentally friendly, robustly water-resistant, and highly breathable fibrous textiles. *ACS Nano* **2019**, *14*, 1045–1054. [CrossRef] [PubMed]
55. Deyab, N.M.; Ekram, B.; Badr, K.R.; Abd El-Hady, B.M.; Allam, N.K. Antiviral electrospun. polyamide three-layered mask filter containing metal oxide nanoparticles and black seed oil. *ACS Omega* **2022**, *7*, 44438–44447. [CrossRef] [PubMed]
56. Hrouda, A.; Jirkovec, R.; Safka, J.; Vanierschot, M.; Denis, K.; Capek, L. Standardized tensile testing of electrospun PA6 membranes via the use of a 3D printed clamping system. *Textile Res. J.* **2022**, *92*, 2298–2305. [CrossRef]
57. Han, P.; Gomez, G.A.; Duda, G.N.; Ivanovski, S.; Poh, P.S. Scaffold geometry modulation of mechanotransduction and its influence on epigenetics. *Acta Biomater.* **2023**, *163*, 259–274. [CrossRef] [PubMed]
58. Islam, M.S.; McCutcheon, J.R.; Rahaman, M.S. A high flux polyvinyl acetate-coated electrospun nylon 6/SiO_2 composite microfiltration membrane for the separation of oil-in-water emulsion with improved antifouling. *J. Membr. Sci.* **2017**, *537*, 297–309. [CrossRef]
59. Chen, Y.; Tang, X.; Gao, X.; Zhang, B.; Luo, Y.; Yao, X. Antimicrobial property and photocatalytic antibacterial mechanism of the TiO_2-doped SiO_2 hybrid materials under ultraviolet-light irradiation and visible-light irradiation. *Ceram. Int.* **2019**, *45*, 15505–15513. [CrossRef]
60. Qin, Q.; Sun, T.; Yin, W.; Xu, Y.; Qin, Q.; Sun, T.; Yin, W.; Xu, Y. Rapid and efficient removal of methylene blue by freshly prepared manganese dioxide Rapid and efficient removal of methylene blue by freshly prepared manganese dioxide. *Cogent Eng.* **2017**, *7*, 1345289. [CrossRef]
61. Çoruh, S.; Geyikçi, F.; Nuri Ergun, O. Adsorption of basic dye from wastewater using raw and activated red mud. *Environ. Technol.* **2011**, *32*, 1183–1193. [CrossRef] [PubMed]
62. Sodkouieh, S.M.; Kalantari, M.; Shamspur, T. Methylene blue adsorption by wheat straw-based adsorbents: Study of adsorption kinetics and isotherms. *Korean J. Chem. Eng.* **2023**, *40*, 873–881. [CrossRef]
63. Tan, Y.; Lv, X.; Wang, W.; Cui, C.; Bao, Y.; Jiao, S. Surface-functionalization of hydrogen titanate nanowires for efficiently selective adsorption of methylene blue. *Appl. Surf. Sci.* **2023**, *615*, 156265. [CrossRef]
64. Chung, J.; Sharma, N.; Kim, M.; Yun, K. Activated carbon derived from sucrose and melamine as low-cost adsorbent with fast adsorption rate for removal of methylene blue in wastewaters. *J. Water Process Eng.* **2022**, *47*, 102763. [CrossRef]
65. Fiaz, R.; Hafeez, M.; Mahmood, R. Ficcus palmata leav es as a low—Cost biosorbent for methylene blue: Thermodynamic and kinetic studies. *Water Environ. Res.* **2019**, *91*, 689–699. [CrossRef]